Turquoise magic wavelength of the ^{87}Sr clock transition

G. Kestler,[1] R.J. Sedlik,[1] E.C. Trapp,[2] M.S. Safronova,[3] and J.T. Barreiro[1,*]

[1] *Department of Physics, University of California San Diego, La Jolla, California 92093, USA*

[2] *Department of Physics, Harvard University, Cambridge, Massachusetts 02138, USA*

[3] *Department of Physics and Astronomy, University of Delaware, Newark, Delaware 19716, USA*

(Received 9 July 2025; revised 22 October 2025; accepted 22 December 2025; published 22 January 2026)

Optical lattice clocks of fermionic strontium offer a versatile platform for probing fundamental physics and developing quantum technologies. The bivalent electronic structure of strontium gives rise to a doubly forbidden atomic transition that is accessible due to hyperfine mixing in fermionic strontium-87, thus resulting in a submillihertz natural linewidth. Currently, the most accurate optical lattice clocks operate on this narrow transition by tightly trapping strontium-87 atoms in a *magic* optical lattice at 813 nm. Magic wavelengths occur where the Stark shifts of both the ground and excited states are equal, thus eliminating any position- and intensity-dependent broadening of the corresponding transition. Theoretical calculations of the electronic structure of strontium-87 have also predicted another magic wavelength of the clock transition at 497.01(57) nm. In this work, we experimentally measure the magic wavelength to be 497.4364(4) nm. Compared to the 813-nm magic wavelength, 497 nm is closer to the strong 461-nm dipolar transition of strontium, resulting in an order-of-magnitude increase in atomic polarizability and deeper traps with less optical power. The proximity to the 461-nm transition also leads to an enhanced sensitivity of 334(10) Hz/(nm E_R) at the magic wavelength.

DOI: 10.1103/rp9f-664g

I. INTRODUCTION

Cold-atom experiments provide key insights into fundamental physics and serve as a platform for quantum science and technologies. Gases of neutral atoms are laser-cooled to micro- and nanokelvin temperatures and optically trapped in engineered light fields for matter-wave interferometers [1–3], neutral atom-based quantum computers [4,5], and precision atomic clocks [6–9]. Each platform is developed around the electronic properties of an atomic species; in particular, bivalent alkaline-earth atoms offer a unique toolbox.

Among the alkaline-earth atoms, strontium is particularly well suited for emulating many-body physics and applications in quantum science and technology. With two-valence electrons, strontium's electronic structure offers broad (approximately 30 MHz) and narrow (approximately 7 kHz) linewidth atomic transitions for laser cooling, which are utilized to produce atomic clouds at temperatures near 1 μK with only a two-stage magneto-optical trap (MOT). Loading these cold atoms into optical lattices and engineered light fields requires less power and shallower traps than other atomic species [10]. With the bosonic isotope, ^{88}Sr, the 7.4-kHz intercombination line is used for sensitive matter-wave interferometry [11] as well as in high-resolution spectroscopy for determining light shifts [10,12] and probing surface interactions, such as the Casimir-Polder effect [13,14]. Arrays of atomic clocks have also been implemented using the doubly forbidden submillihertz "clock" transition of strontium-88 [15]. Precise optical control of the fermionic isotope, ^{87}Sr, which has a nuclear spin of 9/2, realized fermionic spin-momentum and spin-color lattices for many-body physics [16,17], inspired quantum computers with fermionic hardware [18], and enabled precision spectroscopy for the most accurate atomic clocks to date [9].

Atomic clocks of ^{87}Sr rely on recoil-free spectroscopy through the tight confinement of the cold atoms in a deep optical lattice. The bivalent electronic structure of strontium gives rise to a spherically symmetric ground state with no angular momentum, $J = 0$. The $^1S_0$–$^3P_0$ transition, with $J = 0 \rightarrow J' = 0$, is thus doubly forbidden by both the spin and angular momentum selection rules [19,20]. However, this transition is optically accessible by hyperfine mixing in the fermionic isotopes [7] or magnetic-field-induced mixing in the bosonic isotopes [21]. High-resolution "clock" spectroscopy is performed

*Contact author: barreiro@ucsd.edu

by exciting the lattice-trapped atoms into the long-lived $^3P_0$ state before repumping them back to the $^1S_0$ ground state. The highly sensitive spectroscopic platform has measured fermionic interactions [22], gravitational redshift at the millimeter scale [23], and black-body radiation shifts [9].

Optical lattices generate an energy potential for the atoms through an ac Stark shift, where the atoms experience an induced dipole moment from the time-varying trapping field. The direction and strength of the energy shift depend on the trapping field intensity and the atomic polarizability, which in turn depend on the wavelength and the electronic energy state of the atoms. If the ground state, $^1S_0$, and the excited state, $^3P_0$, of the "clock" transition experience different energy shifts, the transition resonance will depend on the field intensity at the atom position, leading to an undesired broadening. Employing a *magic* wavelength for the optical lattice ensures both the ground and excited state experience the same atomic polarizability and ac Stark shift, thus preserving the narrow "clock" transition. Optical traps at 813.428 nm are currently the standard for magic "clock" lattices; however, the ground- and excited-state atomic polarizability at 813 nm is only 247.5(2) a.u. [24]. By selecting a magic wavelength closer to the 461-nm transition, such as 497 nm, the ground- and excited-state atomic polarizability increases by nearly an order of magnitude to approximately 1350 a.u., allowing for an equal and opposite reduction in optical intensity to achieve the same trap depths. Recently, a magic wavelength of the "clock" transition for bosonic strontium, ^{88}Sr, was measured at 477 nm [25].

Here, we experimentally confirm a predicted magic wavelength of the "clock" transition for fermionic strontium near 497 nm, benchmarking the accuracy of the atomic theory. The polarizability of the $^3P_0$ state near 497 nm is dominated by the contribution of the $5s5d\ ^3D_1$–$5s5p\ ^3P_0$ and $5p^2\ ^3P_1$–$5s5p\ ^3P_0$ matrix elements. Knowledge of these matrix elements is crucial for further refining the blackbody-radiation shift estimates in the Sr clock at room temperature. The excellent agreement between the theoretical and experimental values demonstrates the validity of the theoretical values for these matrix elements and uncertainty estimates.

II. THEORY

To compute the Sr magic wavelength, we calculate the $^1S_0$ and $^3P_0$ polarizabilities using a combined configuration interaction (CI) and coupled-cluster approach. We refer to this method as CI+all-order approach [26–29]. In this method, the energies and wave functions are determined from the time-independent multiparticle Schrödinger equation

$$H_{\rm eff}(E_n)\Phi_n = E_n\Phi_n, \tag{1}$$

where the effective Hamiltonian is defined as

$$H_{\rm eff}(E) = H_{\rm FC} + \Sigma(E), \tag{2}$$

where $H_{\rm FC}$ is the Hamiltonian in the frozen core approximation and Σ is the energy-dependent correction, which takes into account virtual core excitations computed using the linearized coupled-cluster method [26,29]. The scalar dynamic polarizability $\alpha(\omega)$ separates into three parts,

$$\alpha(\omega) = \alpha_v(\omega) + \alpha_c(\omega) + \alpha_{vc}(\omega), \tag{3}$$

where α_v is the valence polarizability and α_c is the ionic core polarizability. A small term α_{vc} is included due to the presence of two-valence electrons to restore the Pauli principle by slightly modifying the core polarizability. The α_c and α_{vc} terms were evaluated in the random-phase approximation (RPA).

The valence part of the polarizability is determined by solving the inhomogeneous equation of perturbation theory in the valence space. It is approximated as

$$(E_v - H_{\rm eff})|\Psi(v,M')\rangle = D_{{\rm eff},q}|\Psi_0(v,J,M)\rangle \tag{4}$$

for a state v with the total angular momentum J and projection M [30]. $D_{\rm eff}$ is the effective dipole operator that includes RPA corrections. This approach accounts for all intermediate, high-lying discrete states and the continuum, and provides the total theory value for the valence scalar polarizability at a given frequency.

We also repeat all computations with Σ constructed using second-order many-body perturbation theory to assess uncertainties (CI+MBPT approach), as this provides an estimate of omitted correlation corrections when no experimental matrix elements are available.

To improve the accuracy of the computations, we recalculate all the dominant contributions to all polarizabilities (for each wavelength point) using the experimental energies [31] and recommended values of the electric dipole matrix elements, where available, using the formula [32]

$$\alpha_{0v} = \frac{2}{3(2J+1)}\sum_k \frac{\langle k\,\|D\|\,v\rangle^2(E_k - E)}{(E_k - E)^2 - \omega^2}, \tag{5}$$

where ω is assumed to be at least several linewidths off resonance with the corresponding transitions and $\langle k\,\|D\|\,v\rangle$ are the reduced electric-dipole matrix elements.

We plot the final values of the $^1S_0$ and $^3P_0$ polarizabilities in Fig. 1 and determine the magic wavelength to be 497.01(57) nm. To estimate the uncertainty in the value of the magic wavelength, we also plot $\alpha + \delta\alpha$ and $\alpha - \delta\alpha$ values of the $^1S_0$ and $^3P_0$ polarizabilities. The uncertainty is determined as the largest difference of the $\alpha + \delta\alpha$ and $\alpha - \delta\alpha$ crossings with the central crossing that determines the magic wavelength.

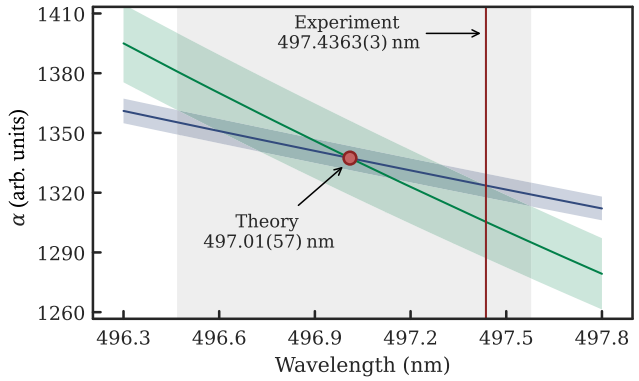

FIG. 1. Theoretical prediction of the $^1S_0$ ground-state (blue) and $^3P_0$ excited-state (green) polarizabilities. The blue (green) shading represents the theoretical uncertainties $\delta\alpha$ in the ground-state (excited-state) polarizabilities. The magic wavelength occurs at their overlap (red circle at 497.01(57) nm), with the uncertainty represented by the gray shaded area. The experimental value (red line at 497.4364(4) nm) falls within the theoretical prediction.

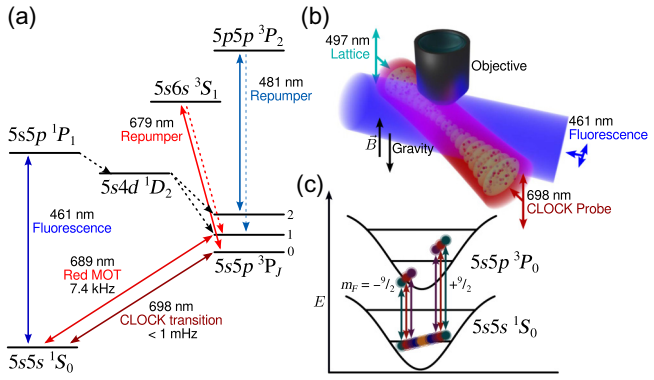

FIG. 2. (a) Relevant levels and transitions for ^{87}Sr used in the experiment. (b) Experimental setup of the optical lattice at 497 nm. The polarization of the optical lattice and "clock" probe is vertical and parallel to the direction of gravity. Fluorescence is collected from an objective (NA = 0.8) and driven by a horizontally polarized 461-nm probe beam operating on the strong dipolar transition. An approximately 17-G magnetic field, $\vec{B}$, is applied along the direction of gravity and sets the quantization axis parallel to the probe polarization for spin-resolved spectroscopy. (c) The atoms are adiabatically loaded into the lowest vibrational energy level of the lattice. A resonant laser drives π-transitions for each $m_F = \{\pm 5/2, \pm 7/2, \pm 9/2\}$ sublevel between the $5s^2\ ^1S_0$ ground state and the $5s5p\ ^3P_0$ excited state.

III. EXPERIMENTAL SETUP

Cold-atom experiments are typically performed in cycles that start from a hot gas of atoms and progress through several stages of laser cooling, culminating in a destructive measurement of the atom number. The experimental cycle in this work is adapted from previous work with this apparatus [16] that has a standard two-stage MOT operating first on the $^1S_0$–$^1P_1$ transition at 460.86 nm [See Fig. 2(a)]. The second stage MOT uses the narrow-line $^1S_0(F = 9/2)$–$^3P_1(F = 11/2)$ transition at 689.4 nm and a weaker *stirring* beam resonant with the $^1S_0(F = 9/2)$–$^3P_1(F = 9/2)$ transition to mix the m_F substates [33]. A high-NA objective in the downward MOT path produces asymmetric beams in the vertical direction, introducing a small degree of spin polarization and resulting in unequal populations of the plus and minus Zeeman spin-projected states. However, all 10 spin states are still present. We load the roughly 1 μK atoms into a crossed dipole trap and perform evaporative cooling for 5.43 s to reach a degenerate Fermi gas (DFG) with $T/T_F = 0.30(1)$.

The DFG is loaded adiabatically into a horizontally oriented, retroreflected optical lattice at approximately 497 nm. We copropagate a narrow-linewidth, cavity-locked resonant probe beam with the optical lattice to interrogate the $^1S_0$–$^3P_0$ doubly forbidden "clock" transition of the trapped atoms [see Fig. 2(b)]. Both lattice and probe beams are vertically polarized, parallel to the magnetic field, to ensure that we drive π-transitions where the ground and excited substates are equivalent ($m_F = m_{F'}$).

Atoms in the lattice experience a level-dependent Stark shift induced by the time-oscillating electric field of the trapping laser light. Determination of this light-induced Stark shift from the lattice is accomplished by performing narrow-linewidth spectroscopy on the $^1S_0$–$^3P_0$ transition at various trapping wavelengths and optical powers. Directly measuring fluorescence of the weak "clock" transition is difficult in our setup, so we collect fluorescence on the strong 461-nm transition instead. We begin by driving the transition of interest ($^1S_0$–$^3P_0$) to shelve a fraction of the trapped atoms in the long-lifetime excited state. Next, we remove any residual ground-state atoms from the lattice using 461-nm light resonant with the $^1S_0$–$^1P_1$ transition. The shelved atoms are unaffected during this step. Finally, the shelved atoms are repumped from the excited state atoms back to the ground state via the $5s6s\ ^3S_1$ and $5p^2\ ^3P_2$ states, where they are ultimately probed with 461-nm light. When the original shelving light is resonant with the $^1S_0$–$^3P_0$ transition, a maximal fraction of atoms will be shelved and repumped during the sequence, thus leading to a peak in the final 461-nm fluorescence signal. If the original shelving light is far detuned from resonance, no atoms are observed in the final stage and the fluorescence signal is zero.

With high-resolution spectroscopy, we can precisely measure the differential shift of the $^1S_0$–$^3P_0$ transition at various trapping wavelengths of the optical lattice. Furthermore, when atoms are optically trapped in a magic wavelength lattice, the transition resonance is independent of the trap depth. We vary both the optical trap depth and wavelength under two unique experimental conditions using a "full-spin" and "single-spin" configuration. The

former uses a broader spectroscopy across a wider range of trapping wavelengths, but allows us to cancel magnetic field effects. The latter setup provides a more sensitive measurement by decreasing the spectroscopy linewidth and spin-polarizing the sample.

In the full-spin configuration, we first measure the magic wavelength using six spin states and a power-broadened spectroscopy sequence. For multiple wavelengths from 497.2 nm to 497.55 nm, we load atoms into the lattice at various final depths from $20E_R$ to $44E_R$, where $E_R = (\hbar k)^2/2m$ is the recoil energy associated with a lattice photon. We apply a magnetic field of approximately 17 G along gravity, and perform high-resolution spin-resolved spectroscopy of the $\pm 9/2, \pm 7/2$, and $\pm 5/2$ transitions [see Fig. 2(c)], once for multiple lattice trap depths, following the sequence detailed above. In this first, broader measurement configuration, we apply a 400-ms saturated probe pulse ($\Omega = 2\pi \times 11(1)$ Hz, see Appendix C) to transfer atoms into $^3P_0$, with the probing laser frequency-locked to an ultrastable cavity (Stable Laser Systems, specified linewidth of 1 Hz). After removing residual ground-state atoms, 10 ms of repumper light at approximately 679 nm and approximately 481 nm is applied to cycle shelved atoms back into the ground state for readout. We then average each relative substate ($+9/2$ with $-9/2$, $+7/2$ with $-7/2$, $+5/2$ with $-5/2$) to cancel magnetic field and nonlinear polarization effects. The resulting slope of the linear relationship between optical trap depth and spectroscopic shift provides the differential Stark-shift coefficient (DSSC), which is zero at the magic wavelength.

Following the initial determination, we perform a second, more precise measurement of the magic wavelength by spin-polarizing the atomic cloud to the $+9/2$ spin state and reducing the probe power to reach a Fourier-limited linewidth of approximately 20 Hz for a π-pulse time of 47 ms. We reduce the range of trapping wavelengths from 497.432 nm to 497.439 nm and the trapping depths from 24 E_R to 44 E_R. Instead of the single-sample full-spin measurement in the initial experiment, we repeat the single-spin spectroscopy measurement three times for every trapping wavelength and power, increasing the confidence of this more precise measurement.

IV. RESULTS

Between the two experiments, the "full-spin" configuration provides a more general result on the way to making the more precise measurement. For this situation, Fig. 3(a) illustrates an example spectroscopy result at an off-magic trapping wavelength of 497.35 nm. The π-polarized probe light ensures we are driving the $^1S_0(m_F = \pm 5/2, \pm 7/2, \pm 9/2)$–$^3P_0(m_F = \pm 5/2, \pm 7/2, \pm 9/2$ π-transitions [see Fig. 2(c)]. Different peak heights between the $+5/2$, $+7/2$, and $+9/2$ are proportional to the Clebsch-Gordon coefficients, while the

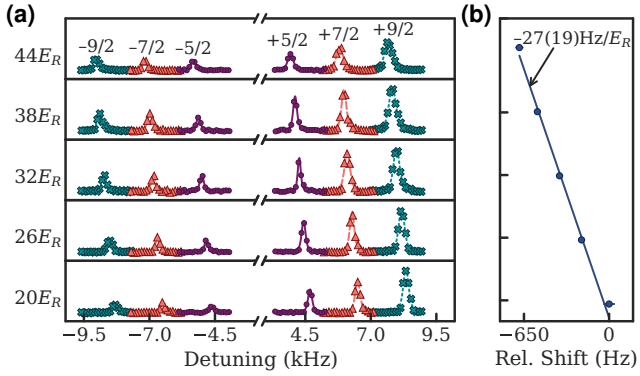

FIG. 3. Measurement of the differential Stark shift at 497.35 nm. (a) Narrow line spectroscopy of the $m_F = \{\pm 5/2, \pm 7/2, \pm 9/2\}$ spin states. Asymmetric vertical MOT beams produce a slightly spin-polarized sample before loading into the lattice, resulting in uneven excited-state populations of the $\pm m_F$ spin states. (b) Linear relationship of the resonant shift to the lattice trap depth. The differential Stark shift is given by the inverse of the slope in Hz/E_R.

smaller populations of the $-5/2$, $-7/2$, and $-9/2$ Zeeman substates are a result of the asymmetric MOT beams, which give rise to a slight spin polarization of the atomic cloud.

We cancel any magnetic field noise by averaging the resonance of alternating-sign m_F states. The quantization axis at the atoms is set along the direction of gravity by a 17.03(5)-G magnetic field generated by the MOT coils in a Helmholtz configuration. The approximately 109-Hz/G [34] differential level shift between the $^1S_0$ and $^3P_0$ states gives rise to a 1.856(5)-kHz separation of neighboring Zeeman substates. Additionally, the spectral lines are broadened to approximately 180 Hz, due to saturated probe power and the ac Stark shift. The latter occurs because the state-dependent energy shifts differ depending on the atoms' positions within the Gaussian radial profile of the lattice. By varying the total trapping depth, a linear relationship between Stark shift and trap depth can be extracted as the DSSC for a single wavelength [see Fig. 3(b)]. In Fig. 4, we repeat the DSSC measurement for different trapping wavelengths and extract the magic wavelength to be 497.434(2) nm for the full-spin configuration, with a sensitivity of 334(10) Hz/(nm E_R).

We now implement the more precise experiment using a single spin state. After evaporative cooling of the DFG, we remove m_F substates by applying spin-selective kick-out pulses [16]. The remaining atoms in the optical lattice are thus purely in the $m_F = +9/2$ substate (see Appendix A 2). Reducing the probe power during the spectroscopy sequence, we use a π-pulse of 47 ms owing to a Fourier-limited linewidth of approximately 20 Hz. This allows us to determine the magic wavelength more precisely at 497.4364(4) nm as shown in Fig. 4 (inset).

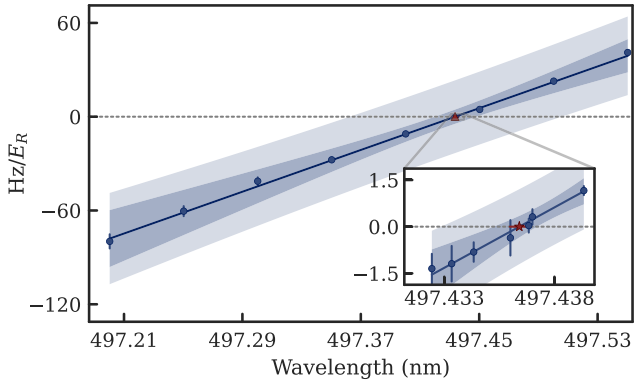

FIG. 4. Differential Stark shifts at various wavelengths. The linear relationship provides a sensitivity of 334(10) Hz/(nm E_R) and the magic wavelength is given at 497.434(2) nm (red triangle). For the inset, we spin-polarize to the $m_F = +9/2$ state and decrease the linewidth to 20 Hz, measuring a magic wavelength of 497.4364(4) nm indicated by the red star. In both plots, the light-shaded regions are the 95% confidence interval and the dark-shaded regions are the 95% prediction interval (see Appendix A 2).

Density-dependent spectroscopic shifts can contribute to a discrepancy between the full-spin and single-spin configurations, since the atomic density in a lattice site varies by approximately 25% across the range of trap depths. These shifts are typically of the order of 1 Hz [35], an order of magnitude less than the fit uncertainty, and do not affect a single DSSC measurement. We confirm there are no inconsistencies between the full- and single-spin setups by performing the Fourier-limited spectroscopy sequence without spin polarization (see Fig. 5). Furthermore, since the single-spin sample prevents us from canceling magnetic field effects, we confirm the precise, intensity-independent result for the $+7/2$ spin state as well (Fig. 5).

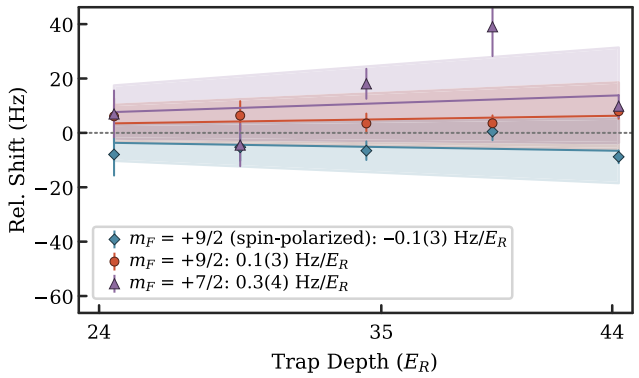

FIG. 5. Demonstration of zero shift for a wide range of trap depths from $24E_R$ to $44E_R$, confirming the magic wavelength at 497.4364(4) nm. The shaded areas represent the uncertainty in the slope, indicating that the zero-slope line falls within this uncertainty.

TABLE I. Contributions to systematic errors in the magic wavelength measurement (see main text). All contributions are included in the final report for both the full-spin configuration (497.434(2) nm) and the single-spin configuration (497.4364(4) nm).

Contribution	Offset	Uncertainty
"Clock" laser drift	+5.9 (mHz/s)	1.8
Lattice AOM	−0.07 (pm)	0.01
Wave meter	+0.4 (pm)	0.1

For both measurement configurations, various systematic errors contribute to the overall error (see Table I). There is a slow drift in the ultrastable cavity, which cascades to the probing laser frequency and thus changes the relative spectroscopy results over time. Since the data point in Fig. 3 takes around 4 h to complete, we reduce the drift rate to 5.9(18) mHz/s and actively correct for the drift during data collection (see Appendix A 1). We determine the wavelength of our optical lattice via a high-finesse WSU-2 wave meter calibrated to the 7.4-kHz $^1S_0$–$^3P_1$ transition at approximately 689 nm. However, calibrating the wave meter at 689 nm introduces a +0.4(1)-pm offset in wavelengths close to 500 nm [10]. Furthermore, the wavelength of the lattice light is measured before it passes through an acousto-optical modulator (AOM) used for intensity stabilization. The +80-MHz AOM introduces a −0.07(1)-pm wavelength shift between the measured and actual values at the atoms. All of these errors are accounted for and propagated through to the final reports of 497.434(2) nm and 497.4364(4) nm.

Another possible error arises in the full-spin measurement of our first experiment. At wavelengths far detuned from magic, the ac Stark shift also introduces a slight asymmetry in the lineshape profile at deeper lattice depths due to any deviation from a perfectly symmetrical Gaussian profile. This effect causes a small divergence from the linear model far from the magic wavelength, which is incorporated in the error of the linear fit. The single-spin, more precise measurement of the magic wavelength avoids this issue by limiting the measurements in a regime where the Stark shift is less than about 1 Hz/E_R.

V. OUTLOOK

In this work, we report on a magic wavelength of the ultranarrow strontium "clock" transition at 497.4364(4) nm. Efforts to produce more accurate clocks rely on close collaboration between theoretical calculations and experimental techniques to reduce the observed linewidth and eliminate shifts and broadening effects [8,9]. Measurement

of the magic wavelength offers insight into theoretical calculations of dipole matrix elements for ^{87}Sr.

Observing the "clock" transition in a magic optical lattice at 497 nm marks an experimental departure from the prevalent 813-nm optical traps with several possible avenues to pursue, including arrays of atomic clocks [15,18], super- and subradiant phenomena [36], and deeply degenerate Fermi gases in optical tweezers [37]. Specifically, for arrays of atomic clocks implemented with tightly focused optical tweezers, the smallest waists achievable with high-NA objectives are diffraction-limited and proportional in size to the wavelength of light. For 497-nm light, the smallest spot sizes are $497/813 \approx 0.6$ times smaller and the atomic polarizability is approximately 5 times larger [24]. Since optical trap depths are proportional to α/ω_0^2, where α is the atomic polarizability and ω_0 is the beam waist, one can expect an improvement of about $14\times$ in trapping efficiency for equivalent setups. Despite the increase in trapping efficiency, the wavelength proximity to the dipole transition at 461 nm presents possible losses due to increased scattering. At 497 nm we observe a ground-state trap lifetime of 8(2) s (see Appendix B) compared to the vacuum lifetime of 64(3) s observed in Ref. [9]. However, laser cooling the trapped atoms can mitigate these losses and recover a longer lifetime.

Unlike trapping lifetime, the fundamental diffraction-limited spot size is constant for a given wavelength. Thus, the smaller spot size allows for $3\times$ more traps in the same area, leading to a more scalable and efficient platform for optical clock arrays of single fermions, which can be used to implement fermionic quantum computers [18]. The tightly focused optical tweezers also provide a small trapping volume, which can adiabatically load ultracold atoms from the crossed dipole trap. The transfer increases the Fermi energy while keeping the atom temperature relatively constant, thus compressing the Fermi gas and enhancing the degeneracy parameter of the cloud [37]. In terms of optical lattice clocks, the separation between neighboring sites in a 497-nm lattice is approximately 248.5 nm. With a transition wavelength of 698 nm, this falls in a regime to study super- and subradiant phenomena with optical clocks, even more so than the approximately 400-nm spacing in 813-nm optical lattices [36].

ACKNOWLEDGMENTS

The National Science Foundation Awards No. 1752630 and No. 2412662 supported the experimental work, while the Office of Naval Research Grant No. N000142512105 supported the theoretical work.

DATA AVAILABILITY

The data that support the findings of this article are openly available [39].

APPENDIX A: SPECTROSCOPY MEASUREMENT

1. Broad scans

Since each experimental run is approximately 10 s, a single data point in Fig. 4 takes approximately 4 h. Long-term frequency drift in the laser frequency can cause a systematic error in the spectroscopy measurements. We measure a drift in the ultrastable cavity of the order of 3 kHz per day or 23 mHz/s and implement feedforward stability by adjusting the laser frequency into the cavity with an electro-optical modulator updated every second. Feedforward correction risks accidentally narrowing the transition during high-resolution spectroscopy scans, so we partially implement the correction amount to ensure the drift rate is less than 5 mHz/s. The spectroscopic shift at each trap depth is varied out of order, measuring $44E_R$, $32E_R$, $20E_R$, $26E_R$, and $38E_R$, followed by a second reference at $44E_R$. Any residual drift between the first and last $44E_R$ spectroscopy measurement is accounted for, and the errors are propagated to each data point prior to fitting the line. We also account for magnetic field noise by alternating m_F-substate scans and averaging both to determine the appropriate Stark shift at the given lattice depth.

Each spectroscopy measurement is only performed once throughout the broad scans, and the alternating $m_F = \{\pm 5/2, \pm 7/2, \pm 9/2\}$ states are averaged to determine the center frequency for each $m_F = \{5/2, 7/2, 9/2\}$ state. Then all three m_F substates are further averaged and the original error of the spectroscopy fit is propagated to the error bars in Fig. 3(b). Lastly, the linear fit to Fig. 3(b) provides the value and error for each data point in Fig. 4. Therefore, the uncertainty of each data point in Fig. 4 is entirely derived from the error of the fit and not the error of the data. We use the two-sided 95% Student t-score of 12.71 for $n = 1$ sample size to produce the confidence and prediction intervals.

2. Narrow scans

For the narrower scans used for the inset of Fig. 4, we spin-polarize to the $m_F = +9/2$ substate and measure three cycles through trap depths of $44E_R$, $32E_R$, $20E_R$, $26E_R$, and $38E_R$. Each individual trap depth then has three data points to determine the cavity drift correction, which are averaged for a more precise magic measurement of 497.4363(3) nm. The 95% confidence and prediction intervals utilize the $n = 3$ two-sided Student t-score, since we perform three repeated spectroscopy measurements for each trap depth.

APPENDIX B: LATTICE CALIBRATION

We calibrate the lattice by performing sideband spectroscopy for both the axial and radial sidebands [see Fig. 6(a)] and determining the trap depth as $U_0/E_R =$

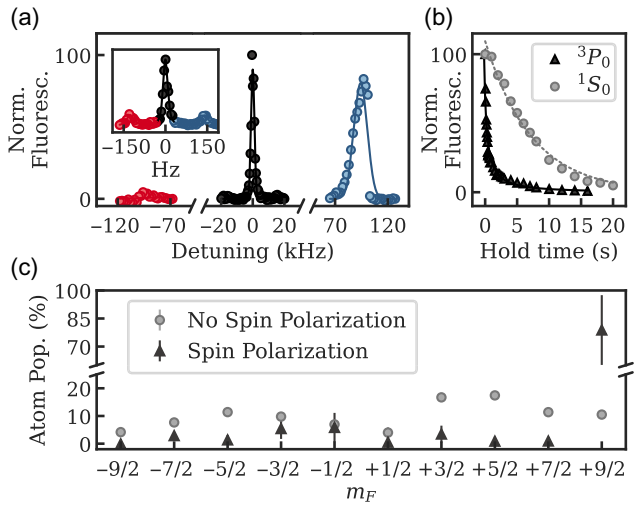

FIG. 6. 497 nm lattice characterization. (a) Axial and radial (inset) sideband spectroscopy. (b) Lifetime measurements for the $^1S_0$ ground state and the $^3P_0$ excited state. The rapid decay of the excited state is due to density-dependent p-wave scattering. The density-independent lifetimes of the ground and excited states are 7.2(4) and 8(2) s, respectively. (c) Atom populations with and without spin polarization. The asymmetric 689 MOT beams create a slight spin polarization in the "no spin polarization" scenario.

$\nu_z^2 m^2 \lambda_T^4/h^2$ and $\nu_z = \sqrt{32\alpha P/4\pi w_0^2 \lambda_T^2 c\epsilon_0 m}$ where the waist is determined by $w_0 = \lambda_T \nu_z/\sqrt{2}\pi \nu_r$. Thus, the trap depth is linear with total power P, and determining the axial and radial trap frequencies for a fixed power is enough to characterize the trap depth at all the powers. The relative heights of the blue and red axial sidebands further confirm that we are indeed loading into the ground state of the lattice.

We also measure the trapping lifetimes for atoms in the ground and excited states [see Fig. 6(b)]. The ground-state lifetime is 8(2) s, but the excited-state lifetime suffers a rapid dropoff within the first 500 ms. This decay agrees well with the two-body loss model [38]

$$\dot{n}_e = -\Gamma n_e - K_{ee} n_e^2$$

rather than an exponential decay, similar to that of the ground state. Fitting to this model for the number of atoms over time, $n_e(t)$, we extract a density-independent lifetime, Γ, of 7.2(4) s, but accurately determining the two-body loss coefficient, K_{ee}, is beyond the scope of this paper. Reducing the atom density and spin-polarizing the trapped atoms recovers an exponential decay for the lifetime.

APPENDIX C: RABI OSCILLATIONS

We calibrate the intensity of the probe beam at the atoms by observing Rabi oscillations at a higher probe power of $P = 253$ μW, which yields a Rabi frequency of

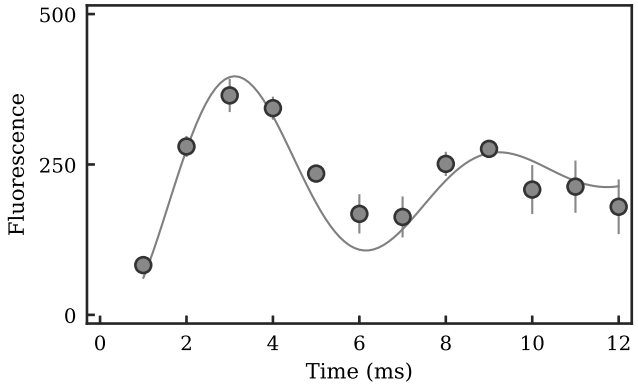

FIG. 7. Rabi oscillations at $\Omega = 169(10)$ Hz calibrated at a probe power of 253 μW. In the experiment, we operate at a probe power of approximately 1 μW, which then corresponds to a Rabi frequency of $\Omega = 2\pi \times 11(1)$ Hz and a π-pulse time of approximately 47 ms.

$\Omega = 169(10)$ Hz (see Fig. 7). Reducing the power to $P' = 1$ μW for the spectroscopy measurements corresponds to scaling the Rabi frequency by $\sqrt{P'/P}$. Our experimental Rabi frequency is then $\Omega = 2\pi \times 11(1)$ Hz.

[1] Y.-J. Wang, D. Z. Anderson, V. M. Bright, E. A. Cornell, Q. Diot, T. Kishimoto, M. Prentiss, R. A. Saravanan, S. R. Segal, and S. Wu, Atom Michelson interferometer on a chip using a Bose–Einstein condensate, Phys. Rev. Lett. **94**, 090405 (2005).

[2] E. R. Moan, R. A. Horne, T. Arpornthip, Z. Luo, A. J. Fallon, S. J. Berl, and C. A. Sackett, Quantum rotation sensing with dual Sagnac interferometers in an atom-optical waveguide, Phys. Rev. Lett. **124**, 120403 (2020).

[3] J. Nemirovsky, R. Weill, I. Meltzer, and Y. Sagi, Atomic interferometer based on optical tweezers, Phys. Rev. Res. **5**, 043300 (2023).

[4] M. Saffman, Quantum computing with atomic qubits and Rydberg interactions: Progress and challenges, J. Phys. B: At., Mol. Opt. Phys. **49**, 202001 (2016).

[5] D. S. Weiss and M. Saffman, Quantum computing with neutral atoms, Phys. Today **70**, 44 (2017).

[6] M. Takamoto, F.-L. Hong, R. Higashi, and H. Katori, An optical lattice clock, Nature **435**, 321 (2005).

[7] M. M. Boyd, A. D. Ludlow, S. Blatt, S. M. Foreman, T. Ido, T. Zelevinsky, and J. Ye, ^{87}Sr lattice clock with inaccuracy below 10^{-15}, Phys. Rev. Lett. **98**, 083002 (2007).

[8] B. J. Bloom, T. L. Nicholson, J. R. Williams, S. L. Campbell, M. Bishof, X. Zhang, W. Zhang, S. L. Bromley, and J. Ye, An optical lattice clock with accuracy and stability at the 10^{-18} level, Nature **506**, 71 (2014).

[9] A. Aeppli, K. Kim, W. Warfield, M. S. Safronova, and J. Ye, Clock with 8×10^{-19} systematic uncertainty, Phys. Rev. Lett. **133**, 023401 (2024).

[10] G. Kestler, K. Ton, D. Filin, M. S. Safronova, and J. T. Barreiro, Magic wavelengths of the Sr ($5s^2\ ^1S_0$–$5s5p\ ^3P_1$)

intercombination transition near the $5s5p\ ^3P_1$–$5p^2\ ^3P_2$ transition, Phys. Rev. A **105**, 012821 (2022).
[11] R. P. del Aguila, T. Mazzoni, L. Hu, L. Salvi, G. M. Tino, and N. Poli, Bragg gravity-gradiometer using the $^1S_0$–$^3P_1$ intercombination transition of ^{88}Sr, New J. Phys. **20**, 043002 (2018).
[12] G. Kestler, Toward ultracold strontium on nanophotonics, Master's thesis, University of California San Diego, 2019.
[13] P. Martin, Development of a strontium magneto-optical trap for probing Casimir-Polder potentials, Ph.D. thesis, University of Oregon, 2017.
[14] E. C. Cook, Laser cooling and trapping of neutral strontium for spectroscopic measurements of Casimir-Polder potentials, Ph.D. thesis, University of Oregon, 2017.
[15] J. P. Covey, I. S. Madjarov, A. Cooper, and M. Endres, 2000-times repeated imaging of strontium atoms in clock-magic tweezer arrays, Phys. Rev. Lett. **122**, 173201 (2019).
[16] P. Lauria, W.-T. Kuo, N. R. Cooper, and J. T. Barreiro, Experimental realization of a fermionic spin-momentum lattice, Phys. Rev. Lett. **128**, 245301 (2022).
[17] C. S. Madasu, C. Mitra, L. Gabardos, K. D. Rathod, T. Zanon-Willette, C. Miniatura, F. Chevy, C. Kwong, and D. Wilkowski, Experimental realization of a SU(3) color-orbit coupling in an ultracold gas, Nat. Commun. **16**, 8448 (2025).
[18] D. González-Cuadra, D. Bluvstein, M. Kalinowski, R. Kaubruegger, N. Maskara, P. Naldesi, T. V. Zache, A. M. Kaufman, M. D. Lukin, H. Pichler, B. Vermersch, J. Ye, and P. Zoller, Fermionic quantum processing with programmable neutral atom arrays, PNAS **120**, e2304294120 (2023).
[19] M. M. Boyd, T. Zelevinsky, A. D. Ludlow, S. Blatt, T. Zanon-Willette, S. M. Foreman, and J. Ye, Nuclear spin effects in optical lattice clocks, Phys. Rev. A **76**, 022510 (2007).
[20] J. Trautmann, D. Yankelev, V. Klüsener, A. J. Park, I. Bloch, and S. Blatt, $^1S_0$–$^3P_2$ magnetic quadrupole transition in neutral strontium, Phys. Rev. Res. **5**, 013219 (2023).
[21] A. V. Taichenachev, V. I. Yudin, C. W. Oates, C. W. Hoyt, Z. W. Barber, and L. Hollberg, Magnetic field-induced spectroscopy of forbidden optical transitions with application to lattice-based optical atomic clocks, Phys. Rev. Lett. **96**, 083001 (2006).
[22] A. Goban, R. B. Hutson, G. E. Marti, S. L. Campbell, M. A. Perlin, P. S. Julienne, J. P. D'Incao, A. M. Rey, and J. Ye, Emergence of multi-body interactions in a fermionic lattice clock, Nature **563**, 369 (2018).
[23] T. Bothwell, C. J. Kennedy, A. Aeppli, D. Kedar, J. M. Robinson, E. Oelker, A. Staron, and J. Ye, Resolving the gravitational redshift across a millimetre-scale atomic sample, Nature **602**, 420 (2022).
[24] M. S. Safronova, S. G. Porsev, U. I. Safronova, M. G. Kozlov, and C. W. Clark, Blackbody-radiation shift in the Sr optical atomic clock, Phys. Rev. A **87**, 012509 (2013).
[25] X. Ma, S. Das, D. Wilkowski, and C. C. Kwong, Magic wavelength at 477 nm for the strontium clock transition, Phys. Rev. Appl. **24**, 064017 (2025).
[26] M. S. Safronova, M. G. Kozlov, W. R. Johnson, and D. Jiang, Development of a configuration-interaction plus all-order method for atomic calculations, Phys. Rev. A **80**, 012516 (2009).
[27] M. S. Safronova, S. G. Porsev, U. I. Safronova, M. G. Kozlov, and C. W. Clark, Blackbody-radiation shift in the Sr optical atomic clock, Phys. Rev. A **87**, 012509 (2013).
[28] A. Heinz, A. J. Park, N. Šantić, J. Trautmann, S. G. Porsev, M. S. Safronova, I. Bloch, and S. Blatt, State-dependent optical lattices for the strontium optical qubit, Phys. Rev. Lett. **124**, 203201 (2020).
[29] C. Cheung, M. G. Kozlov, S. G. Porsev, M. S. Safronova, I. I. Tupitsyn, and A. I. Bondarev, pCI: A parallel configuration interaction software package for high-precision atomic structure calculations, Comput. Phys. Commun. **308**, 109463 (2025).
[30] S. G. Porsev, Y. G. Rakhlina, and M. G. Kozlov, Electric-dipole amplitudes, lifetimes, and polarizabilities of the low-lying levels of atomic ytterbium, Phys. Rev. A **60**, 2781 (1999).
[31] A. Kramida, Yu. Ralchenko, and J. Reader, and the NIST ASD Team, NIST Atomic Spectra Database (version 5.7.1). Available at http://physics.nist.gov/asd. National Institute of Standards and Technology, Gaithersburg, MD (2019).
[32] J. Mitroy, M. S. Safronova, and C. W. Clark, Topical review: Theory and applications of atomic and ionic polarizabilities, J. Phys. B **43**, 202001 (2010).
[33] S. Stellmer, F. Schreck, and T. C. Killian, in *Annu. Rev. Cold At. Mol.* (World Scientific, New York, 2014), p. 1.
[34] S. Campbell, A Fermi-degenerate three-dimensional optical lattice clock, Ph.D. thesis, University of Colorado Boulder, 2017.
[35] A. M. Rey, A. V. Gorshkov, and C. Rubbo, Many-body treatment of the collisional frequency shift in fermionic atoms, Phys. Rev. Lett. **103**, 260402 (2009).
[36] M. A. Norcia, M. N. Winchester, J. R. K. Cline, and J. K. Thompson, Superradiance on the millihertz linewidth strontium clock transition, Sci. Adv. **2**, e1601231 (2016).
[37] L. Viverit, S. Giorgini, L. P. Pitaevskii, and S. Stringari, Adiabatic compression of a trapped fermi gas, Phys. Rev. A **63**, 033603 (2001).
[38] M. Bishof, M. J. Martin, M. D. Swallows, C. Benko, Y. Lin, G. Quéméner, A. M. Rey, and J. Ye, Inelastic collisions and density-dependent excitation suppression in a ^{87}Sr optical lattice clock, Phys. Rev. A **84**, 052716 (2011).
[39] https://doi.org/10.5281/zenodo.18071239